3d Metal Doping of Core@Shell Wüstite@ferrite Nanoparticles as a Promising Route toward Room Temperature Exchange Bias Magnets

Beatrice Muzzi, Martin Albino,* Michele Petrecca, Claudia Innocenti, César de Julián Fernández, Giovanni Bertoni, Clara Marquina, Manuel Ricardo Ibarra, and Claudio Sangregorio*

Nanometric core@shell wüstite@ferrite ($Fe_{1-x}O@Fe_3O_4$) has been extensively studied because of the emergence of exchange bias phenomena. Since their actual implementation in modern technologies is hampered by the low temperature at which bias is operating, the critical issue to be solved is to obtain exchange-coupled antiferromagnetic@ferrimagnetic nanoparticles (NPs) with ordering temperature close to 300 K by replacing the divalent iron with other transition-metal ions. Here, the effect of the combined substitution of $Fe^{(II)}$ with $Co^{(II)}$ and $Ni^{(II)}$ on the crystal structure and magnetic properties is studied. To this aim, a series of 20 nm NPs with a wüstite-based core and a ferrite shell, with tailored composition, ($Co_{0.3}Fe_{0.7}O@Co_{0.8}Fe_{2.2}O_4$ and $Ni_{0.17}Co_{0.21}Fe_{0.62}O@Ni_{0.4}Co_{0.3}Fe_{2.3}O_4$) is synthetized through a thermal-decomposition method. An extensive morphological and crystallographic characterization of the obtained NPs shows how a higher stability against the oxidation process in ambient condition is attained when divalent cation doping of the iron oxide lattice with $Co^{(II)}$ and $Ni^{(II)}$ ions is performed. The dual-doping is revealed to be an efficient way for tuning the magnetic properties of the final system, obtaining Ni-Co doped iron oxide core@shell NPs with high coercivity (and therefore, high energy product), and increased antiferromagnetic ordering transition temperature, close to room temperature.

1. Introduction

The tuning of the physical properties of traditional spinel ferrites by coupling them with different magnetic materials at the nanoscale is a promising strategy that has been extensively investigated in the last decade to optimize their behavior for several high-tech applications.[1–4] One of the most interesting phenomenon encountered in coupled systems is the so called exchange bias effect, generally observed in binary systems comprising an antiferromagnetic (AFM) and a ferro(i)magnetic (F(i)M) ordered phases, when they are cooled in the presence of a magnetic field through the Néel temperature of the AFM component.[5] The exchange bias originates from the pinning force exerted by the AFM phase on the magnetic moments in the first atomic layer of the interfaced F(i)M material, leading to an additional unidirectional anisotropy

B. Muzzi
Departament of Biotechnology
Chemistry and Pharmacy
University of Siena 1240
Siena I-53100, Italy

B. Muzzi, C. Innocenti, C. Sangregorio
ICCOM – CNR
Sesto Fiorentino FI I-50019, Italy
E-mail: csangregorio@iccom.cnr.it

B. Muzzi, M. Albino, M. Petrecca, C. Innocenti, C. Sangregorio
Departament of Chemistry "U. Schiff"
University of Florence and INSTM
Sesto Fiorentino FI I-50019, Italy
E-mail: martin.albino@unifi.it

C. d. J. Fernández
IMEM – CNR
Parma I-43124, Italy

G. Bertoni
CNR – Istituto Nanoscienze
Modena I-41125, Italy

C. Marquina, M. R. Ibarra
Instituto de Nanociencia y Materiales de Aragón (INMA)
Consejo Superior de Investigaciones Científicas (CSIC)-Universidad de Zaragoza
Zaragoza 50009, Spain

C. Marquina, M. R. Ibarra
Departamento de Física de la Materia Condensada
Universidad de Zaragoza
Zaragoza 50009, Spain

M. R. Ibarra
Laboratorio de Microscopias Avanzadas (LMA)
Universidad de Zaragoza
Zaragoza 50018, Spain

**ADVANCED
SCIENCE NEWS**
www.advancedsciencenews.com

**NANO · MICRO
small**
www.small-journal.com

energy.[5] This coupling, indeed, entails an extra energy barrier for the F(i)M uncompensated spins, making more difficult to reverse the magnetization toward the direction opposite to the cooling field. The result is an increase of the coercive field (H_C) and a horizontal shift of the hysteresis loop, characterized by the exchange bias field, H_E. The associated increase of the magnetic loop's area corresponds to a higher capability to store magnetic energy, which is the key feature for most of the modern applications of magnetic materials.

As the exchange coupling occurs at the AFM/ F(i)M interface, it is particularly appreciable in core-shell (CS) nanostructures where the interface represents a high percentage of the whole system volume. Since the exchange bias effect is influenced by the quality of the interface, an epitaxial growing between the two lattices is highly recommended. The high similarity in the oxygen ions packing of spinel (S) and rock-salt (RS) lattices makes them useful building blocks to fabricate a high-quality epitaxial nanostructure. These two crystal structures are typical of several transition metal oxides and many examples of such coupled nanosystems have been reported in the literature, the $Fe_{1-x}O@Fe_3O_4$ (AFM@FiM) CS nanoparticles (NPs) being the most investigated.[6–8] For the synthesis of $Fe_{1-x}O@Fe_3O_4$ wüstite@magnetite CS NPs several methodologies have been investigated, and the thermal decomposition has been established as one of the most reproducible approaches to obtain highly crystalline NPs with a precise control on the size, shape, and chemical composition.[9] The thermal decomposition of an organometallic precursor, that is, a metal oleate, in a high boiling solvent forces the reduction of the $Fe^{(III)}$ ions to $Fe^{(II)}$ favoring the growth of the $Fe_{1-x}O$ structure instead of the expected Fe_3O_4 or γ-Fe_2O_3 (maghemite).[10] The partial oxidation of the $Fe_{1-x}O$ surface to Fe_3O_4 leads to a more complex structure which corresponds to a $Fe_{1-x}O@Fe_3O_4$ CS architecture.[11]

A major problem of these Fe-nanostructures is that the exchange-bias effect appears only below the Néel temperature (T_N) of the AFM phase. Since for FeO T_N is 198 K, the exchange-bias takes place well below room temperature hindering its exploitation in most of the proposed applications. Another drawback is the low magnetic anisotropy of iron ions, which leads to low coercive field values and is hardly modulable.

On the other hand, the capability of interface engineering developed in the last decades offers a powerful tool for physical properties control in nanomaterials.[12,13] For example, the tuning of the interface's chemical composition to modify the surface energy level, has proven to be an effective strategy to attain a final system with tailored chemical-physical properties.[14–19] In this respect, $Fe_{1-x}O@Fe_3O_4$ CS nanocrystals,[20–22] offer the possibility to modify their structural and physical properties by tuning the chemical composition by replacing $Fe^{(II)}$ in the RS and S systems with other divalent cations, such as $Zn^{(II)}$,$Ni^{(II)}$, $Mn^{(II)}$, or $Co^{(II)}$. This strategy, largely reported in the literature, is recognized as an excellent method to obtain systems with tailored chemical-physical properties. For instance, the introduction of $Co^{(II)}$, $Ni^{(II)}$, or $Zn^{(II)}$ ions is known to effectively control the magnetic anisotropy and the saturation magnetization (M_S) of S ferrite NPs,[23–26] whereas T_N, of the AFM RS nanostructure, can be tuned by adjusting the divalent metal composition.[27] Following this approach, Lottini et al.[28] synthesized $Co_{0.3}Fe_{0.7}O@Co_{0.6}Fe_{2.4}O_4$ NPs, which, due to the

presence of the high anisotropic $Co^{(II)}$ ions exhibited largely enhanced exchange bias field, H_E (at 5 K, $H_E = 0.86$ T for 9 nm Co-doped CS NPs[28] compared to 0.12 T observed for 16 nm $FeO@Fe_3O_4$[29]) and higher T_N (227 K compared to 198 K for FeO[30]) although still well below room temperature.

A finer tuning of the magnetic properties can be attained by doping with two different metal ions. In this framework, co-substitution with $Co^{(II)}$ and $Ni^{(II)}$ is particularly appealing since it may provide the best trade-off between the appearance of AFM/FM exchange coupling and the ordering temperature of the AFM phase.[27,31] The introduction of $Ni^{(II)}$ is indeed expected to increase the T_N, as T_N for the bulk nickel monoxide (NiO) is 525 K. Moreover, the structural variation in the monoxide lattice is expected to change the magnetic anisotropy of the whole CS system and the spin interactions at the CS interface, leading to a modification of the hysteresis loops shape with an increase of the remanence value.[32] Nevertheless, to the best of our knowledge, the combined effects of $Ni^{(II)}$ and $Co^{(II)}$ doping on the chemical-physical properties of wüstite@magnetite CS NPs has not been explored so far. To fill this gap, in this work we report an investigation on the structural, morphological, and magnetic properties of $Ni_zCo_xFe_{1-x-z}O@Ni_wCo_yFe_{3-y}O_4$ (**NiCoFeO**) CS NPs synthesized by thermal decomposition of mixed metal oleate precursors. In particular, using advanced electron microscopy techniques we managed to determine the ions distribution with atomic resolution and, identifying a well-defined CS interface, we highlighted the crystallographic families of planes involved in the RS and S phases epitaxial growth. In order to better clarify the effect of $Ni^{(II)}$ on the magnetic behavior of the exchange coupled CS nanosystem, a careful comparison with $Fe_{1-x}O@Fe_{3-y}O_4$, (**FeO**) and $Co_xFe_{1-x}O@Co_yFe_{3-y}O_4$ (**CoFeO**) NPs of similar size and prepared by the same techniques, was carried out.

2. Results and Discussion

2.1. Structural and Morphological Characterization

CS metal monoxide@ferrite NPs with variable composition were obtained following a modified procedure from Lottini et al.[28] The synthesis relies on the formation of AFM RS NPs by thermal decomposition of freshly prepared metal oleate precursors in the high boiling solvent docosane ($T_{eb} = 368.7$ °C), in the presence of oleic acid, followed by a controlled oxidation step during the cool-down of the reaction mixture.

Figure 1 shows the Transmission electron microscopy (TEM) images of the obtained samples, consisting of NPs with spherical morphology, mean diameter of ≈20 nm, with a narrow size distribution (±3 nm), for the whole series. **FeO**, **CoFeO**, and **NiCoFeO** NPs are coated by oleate molecules, which was estimated ≈8% w/w by CHN analysis for all the samples. X-Ray diffraction (XRD) patterns (Figure S1, Supporting Information) confirmed the presence of both the RS and the S ferrite phases in each sample.

To investigate the morphology and the crystalline structure of the NPs, ultra-high resolution transmission electron microscopy (UHRTEM) images were acquired, and their local Fast
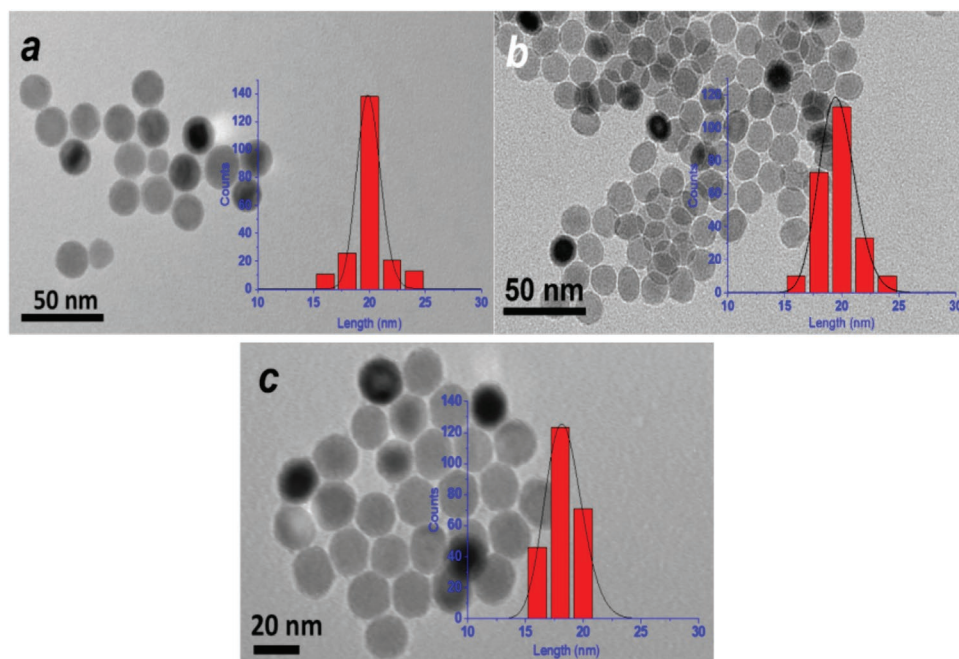
Figure 1. TEM images of a) **FeO**, b) **CoFeO**, and c) **NiCoFeO** NPs with the corresponding size distributions (average size 20 nm for **FeO** and **CoFeO** and 19 nm for **NiCoFeO**).

Fourier Transform (FFT) was analyzed. In **Figure 2**-I, the image of a NP of **NiCoFeO** is shown. Three regions (red squares labeled as a, b, and c) in the core, the shell, and at the interface between the two, respectively, were selected. Their magnifications are shown in Figure 2-II. The FFT analysis, performed on *a* and *b*, reveals the presence of a RS-structure (Figure 2-III(a′)) and of a cubic S-structure (Figure 2-III(b′)), in the core and the shell, respectively. The FFT performed on the interface region

c (red square in Figure 2-II(c)) showed the coexistence of spots related to both the RS and the S ferrite (Figure 2-III(c′)), confirming the presence of a well-defined interface between the two phases and highlighting the crystallographic families of planes {111} involved in the RS and S epitaxial growth. Indeed, the RS-structure of metal monoxide (MO, M = Fe, Co, and Ni) is characterized by octahedral (Oh) sites occupied by $M^{(II)}$ only. Upon oxidation, RS transforms into ferrite which has the cubic
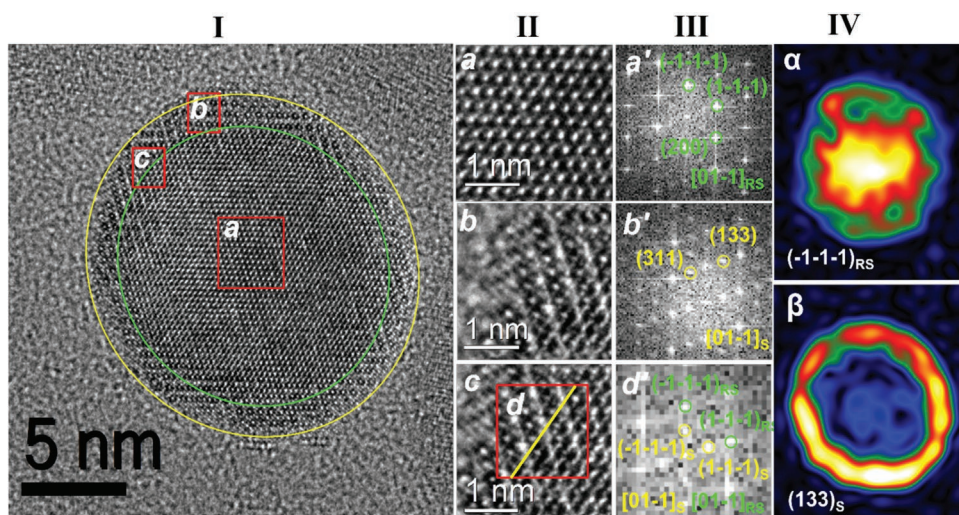

Figure 2. I) HRTEM image of a **NiCoFeO** NP. The red squares a–c) denote regions in the $Ni_{0.17}Co_{0.21}Fe_{0.62}O$ RS core, $Ni_{0.4}Co_{0.3}Fe_{2.3}O_4$ S ferrite shell, and CS interface, respectively. II) Images of the selected regions (a–c) at higher magnification: in (c), the red square (d) indicates the area where the FFT analysis was performed; the yellow line marks the CS interface. III) FFT analysis of the three regions showing the presence of different crystallographic structures: the labeled spots are related to crystallographic planes that can be indexed as: a′) RS phase ($Fm\overline{3}m$), in zone axis $[01-1]_{RS}$, b′) cubic S structure ($Fd\overline{3}m$), $[01-1]_S$, and d′) RS (green) and cubic S oxide (yellow) phases, $[01-1]_{RS}$ and $[01-1]_S$; the presence of both phases confirms a sharp interface. IV) Geometrical phase analysis of the same NP: the yellow and red colors indicate the presence and the localization within the NP of the α) $(-1-1-1)_{RS}$, and β) $(133)_S$, crystallographic directions related to the RS and the S, respectively.

S-structure. Thus, the RS and S structures share the crystallographic directions generated by the Oh point group symmetry ([111]$_{RS}$, [200]$_{RS}$, and [220]$_{RS}$), while the Td sites in the S originate new crystal planes that are not present in the RS phase.[33,34]

The CS structure was also confirmed by geometrical phase analysis (GPA) performed on the same NP: the RS plane (−1−1−1)$_{RS}$ appeared only in the core region of the NP (Figure 2-IV(α)), while the (133)$_S$ plane, related to the S structure, was only found in the shell (Figure 2-IV(β)). The same features were observed also for **FeO** and **CoFeO** (Figures S2,S3, Supporting Information), indicating that all samples comprise two components, a core constituted by a RS metal monoxide and an S ferrite shell. Further analysis of HRTEM images, performed on an average of five **CoFeO** NPs and five **NiCoFeO** NPs, showed the shell was ≈2 nm thick for both NP samples (**Table 1**), with a CS ratio of 0.8 w/w. The same analysis carried out for **FeO** NPs showed that the shell had a thickness of ≈4 nm with a CS ratio of 0.4 w/w.

To investigate the chemical composition and quantify the stoichiometric amount of each element in the three samples, sub nanometric scanning transmission electron microscopy–electron energy loss spectroscopy (STEM-EELS) was performed on a single NP. **Figure 3** shows the color maps corresponding to the distribution of oxygen (red), iron (green), cobalt (blue), and nickel (magenta) for **FeO**, **CoFeO**, and **NiCoFeO**. Qualitatively, these data demonstrated the metal ions were homogeneously distributed in the whole NP, in all the samples.

A quantitative analysis of the relative amount of the different ions was performed from EELS spectra of the STEM-EELS map after principal component analysis (PCA) decomposition. This method has proven very useful to both reduce noise in the spectra and to extract components which are orthogonal in the spatial domain,[35] as in the case of a core and a shell with different compositions. **Figure 4** reports the EELS spectra of the core and the shell of one NP of **NiCoFeO**. The peaks at 708, 779, and 855 eV correspond to the L$_3$ edge of iron, cobalt, and nickel, respectively. The intensity of the Co$^{(II)}$ and Ni$^{(II)}$ peaks increases with respect to the Fe-L$_3$ signal moving from the shell to the core region, underlining a variation in the stoichiometry ratio. From these data a Ni$_{0.17}$Co$_{0.21}$Fe$_{0.62}$O@Ni$_{0.4}$Co$_{0.3}$Fe$_{2.3}$O$_4$ was estimated for the composition of the **NiCoFeO** NPs. Fe$_{0.95}$O@Fe$_3$O$_4$ and Co$_{0.3}$Fe$_{0.7}$O@Co$_{0.8}$Fe$_{2.2}$O$_4$ compositions were similarly estimated for **FeO** and **CoFeO** NPs, respectively (Figures S4,S5, Supporting Information). For **FeO** the formation of maghemite (γ-Fe$_2$O$_3$) was further excluded by EELS and HRTEM analysis (for more details see Supporting Information). These results confirmed that the stoichiometries of the different metal oleates used for the respective syntheses, were preserved in the core region of the NPs. Conversely, the dopants

(Co and Ni ions) to iron ratio in the shell is lower than the nominal value, decreasing from 0.5 to 0.36 for **CoFeO** and from 0.61 to 0.30 for **NiCoFeO**. A similar decrease was observed by Lottini et al. during the synthesis of CS Co$_{0.3}$Fe$_{0.7}$O@Co$_{0.6}$Fe$_{2.4}$O$_4$ NPs. It was associated to the release of cobalt ions to the washing solvent occurring during the oxidation step and recognized as a crucial step toward the formation of the S shell.[28] The relative metal percentages calculated by energy dispersive X-ray fluorescence (EDXRF) on a macroscopic amount of samples, confirmed the stoichiometries obtained by EELS (see Supporting Information).

The electron diffraction (ED) patterns of the three samples (**Figure 5**) show the peaks related to the characteristic planes of the RS structure ($Fm\overline{3}m$); in addition, the reflexions (220)$_S$ and (511)$_S$, distinctive of the S structure ($Fd\overline{3}m$) can be recognized in all the patterns. The intensity ratios of the monoxide peaks ((111)$_{RS}$, (200)$_{RS}$, and (220)$_{RS}$) do not properly match those of the metal monoxide due to the contribution of the S structure planes that partially overlap with the RS ones.

For a quantitative evaluation of the crystal size and lattice parameter a, the full ED patterns were fitted by using a nonlinear least-square fit of Voigt peaks, after the background subtraction by a spline curve fit[36] (Table 1). For FeO NPs, the size of the $Fm\overline{3}m$ crystal core was 10 nm, while the surrounding ferrite shell ($Fd\overline{3}m$) was 3 nm thick. For the doped samples, the RS core size was 18 nm for **CoFeO** and 16 nm for **NiCoFeO**, while the surrounding S phase had a thickness of 2 and 3 nm, respectively. The sizes obtained by the full XRD patterns fit (Table 1), performed using the Pawley method,[37] refining the lattice parameter and the crystal size of both monoxide and S phases, were comparable to the ED fitting results, within the sensitivity of the techniques and the fitting errors

The substitution of Fe$^{(II)}$ ions for Co$^{(II)}$ and/or Ni$^{(II)}$ in the octahedral sites is expected to decrease the unit cell parameter a from 0.4303 nm for FeO[38] to 0.4291 for Co$_{0.3}$Fe$_{0.7}$O and 0.4270 nm for Ni$_{0.17}$Co$_{0.21}$Fe$_{0.62}$O (these values were calculated using the Vegard's law[39] and the bulk CoO and NiO lattice parameters, that is, 0.4262 and 0.4170 nm, respectively).[40,41] The experimental lattice parameters for the **CoFeO** and **NiCoFeO** cores nicely match the expected ones, while for **FeO** cores a smaller unit cell was observed.

The strain related to the replacement of Fe$^{(II)}$ in the octahedral sites of the monoxide structure with smaller divalent cations can affect the magnetic coupling between the cations in the core lattice. The strain maps related to the reflection (200)$_{RS}$ were thus acquired for the three samples (**Figure 6**). These maps allowed us to estimate the displacement of this plane from its reference, that is, average position in the RS structure. The red-green regions are related to the zero-strain value, while

Table 1. Lattice parameter (a) of the RS phase (core) and average crystal size of the core and shell obtained by ED and XRD measurements for **FeO**, **CoFeO**, and **NiCoFeO** (in round brackets the errors of the fitting process are reported). Average size of the core and the shell evaluated by HRTEM.

Samples	ED			XRD			HRTEM	
	Lattice parameter (a) [nm]	Core size [nm]	Shell size [nm]	Lattice parameter (a) [nm]	Core size [nm]	Shell size [nm]	Core size [nm]	Shell size [nm]
FeO	0.4282(1)	10(2)	3(1)	0.4248(2)	12(2)	2(2)	10 ± 3	4 ± 1
CoFeO	0.4288(1)	18(2)	2(1)	0.4274(2)	14(2)	2(1)	16 ± 3	2 ± 1
NiCoFeO	0.4270(1)	16(2)	3(1)	0.4269(2)	16(2)	3(1)	14 ± 3	2 ± 1

ADVANCED
SCIENCE NEWS
www.advancedsciencenews.com

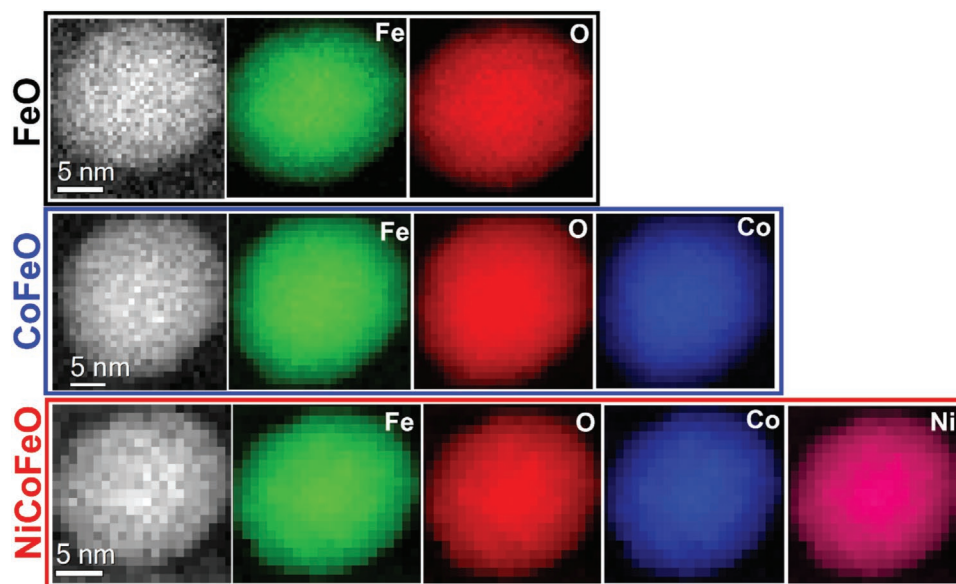NANO · MICRO
small
www.small-journal.com

Figure 3. STEM-EELS mapping and distributions of oxygen (O-K edge, red), iron (Fe-L$_{2,3}$ edge, green), cobalt (Co-L$_{2,3}$ edge, blue), and nickel (Ni-L$_{2,3}$ edge, magenta) inside one NP of **FeO** (black rectangle, top), **CoFeO** (blue rectangle, middle), and **NiCoFeO** (red rectangle, bottom). The color intensity is proportional to the relative concentration of the corresponding ion.

the yellow or blue-black areas correspond to the regions where the planes are tilted (up to 0.3°). The strain mapping confirmed that the doping with Co$^{(II)}$ and Ni$^{(II)}$ of the iron monoxide nanocrystal determined an increase of the lattice strain with respect to the **FeO** NP.

All the data reported so far confirmed the NPs of the three samples have a well-defined CS architecture comprising an AFM RS core surrounded by a ferrite shell with different stoichiometry. FeO has a thicker ferrite shell than that of the NPs of the other two samples. This result is ascribed to the oxidation

process, which propagated from the surface to the inner part of the NP more easily when only iron is present. Indeed, in this latter case, electronic exchange between Fe$^{(II)}$ and Fe$^{(III)}$ can occur, which, conversely, is much less likely when Co$^{(II)}$ or Ni$^{(II)}$ ions are involved. Thus, a smaller shell was obtained when **CoFeO** and **NiCoFeO** NPs were exposed to the ambient conditions, whereas **FeO** NPs have a lower stability, being more prone to oxidation.[34,42,43] The thicker shell caused a higher pressure on the smaller **FeO** core, which underwent a contraction of the RS unit cell. On the other hand, the insertion
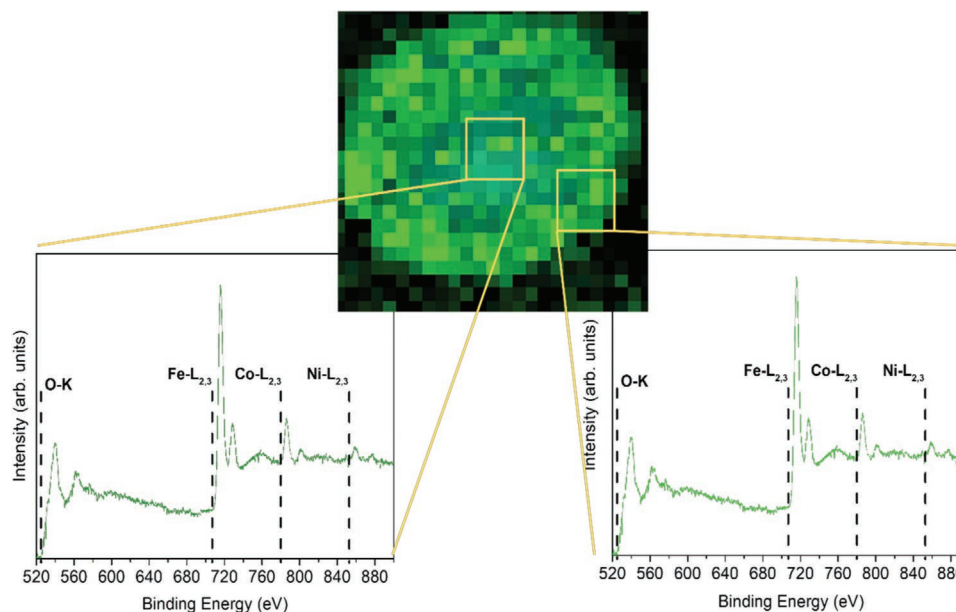

Figure 4. STEM-EELS image of a **NiCoFeO** NP and EELS spectra of the core and shell regions obtained by PCA decomposition.[35] Peaks corresponding to oxygen (O-K edge), iron (Fe-L$_{2,3}$), cobalt (Co-L$_{2,3}$ edge), and nickel (Ni-L$_{2,3}$ edge) are shown in the EELs spectra.
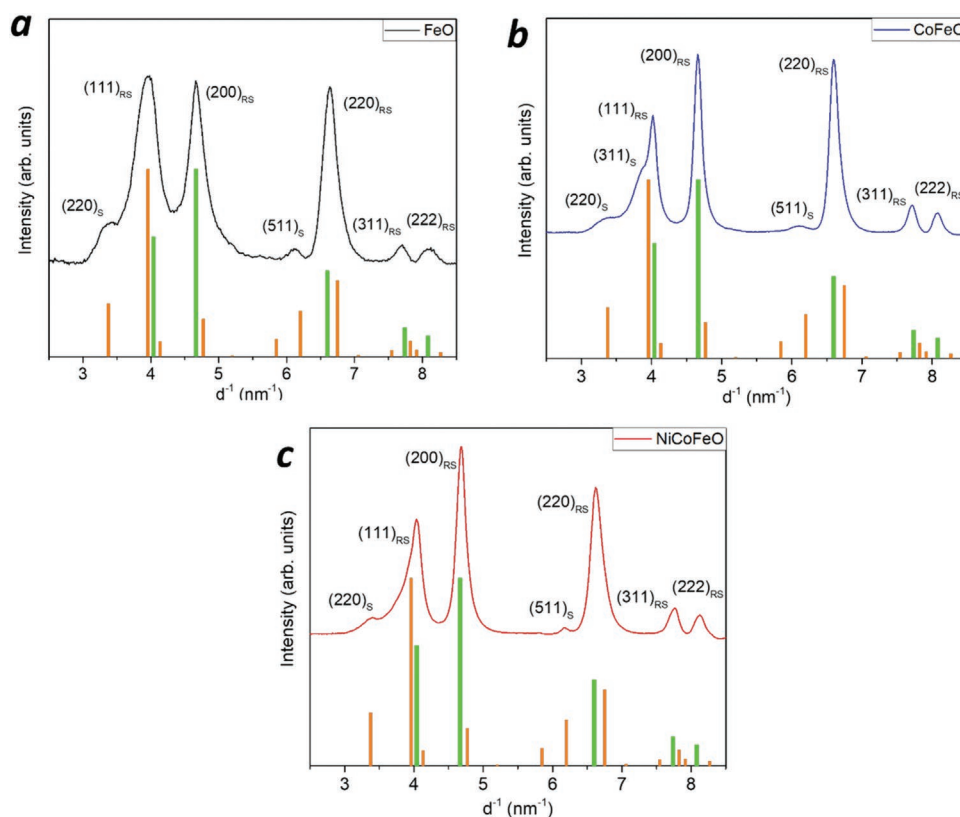
ADVANCED
SCIENCE NEWS

www.advancedsciencenews.com

NANO · MICRO

small

www.small-journal.com

Figure 5. Electron diffraction patterns for a) **FeO**, b) **CoFeO**, and c) **NiCoFeO**. Reference patterns of FeO (JCPDS PDF #73-2144) and Fe$_3$O$_4$ (JCPDS PDF #19-0629) are also shown. RS and S define peaks indexed to the RS and the S structures, respectively.

of Co$^{(II)}$ and Ni$^{(II)}$ in the lattice strongly increased the strain in the monoxide lattice, which led to a broadening of the ED and XRD peaks. According to these observations, it is also important to stress that the cobalt and nickel doping of conventional CS wüstite@magnetite led to the increase of the stability of the NPs against the oxidation process in ambient conditions, avoiding the total structural conversion (oxidation) with long exposure time.
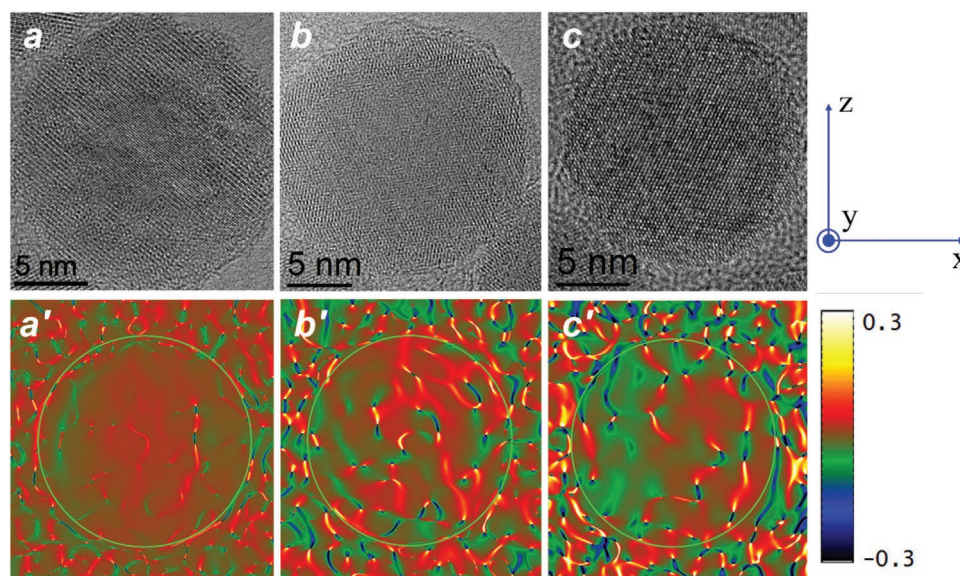
Figure 6. HRTEM Images of samples a) **FeO**, b) **CoFeO**, and c) **NiCoFeO** with the corresponding strain maps (a'–c') ε_{xy} (symmetric shear) calculated from (200)$_{RS}$ reflections, and obtained by GPA analysis. The NP is localized in the green circle; the strain increases passing from red-green region to the yellow-blue one.

ADVANCED
SCIENCE NEWS
www.advancedsciencenews.com

NANO · MICRO
small
www.small-journal.com

2.2. Magnetic Properties of Exchanged Coupled CS Nanoparticles

The substitution of $Fe^{(II)}$ in $Fe_{1-x}O$ or Fe_3O_4 with other divalent cations ($Mn^{(II)}$, $Co^{(II)}$, or $Ni^{(II)}$) is a well-known strategy to tune the magnetic properties of iron oxides.[28,44,45] For example, Fantechi et al. reported how the $Co^{(II)}$ doping of maghemite is able to enhance the saturation magnetization and the magnetic anisotropy.[25] In this work, we exploited this approach for increasing the anisotropy and the ordering temperature of exchanged biased CS NPs by doping with $Co^{(II)}$ and $Ni^{(II)}$ ions, respectively. The temperature dependence of the magnetization of **FeO**, **CoFeO**, and **NiCoFeO** NPs (**Figure 7**a) was measured after zero field cooling (ZFC) and field cooling (FC) procedures, applying a constant high magnetic field of 5 T, to investigate the evolution of the AFM transition temperature without any interference from the blocking process (T_B). In all the cases, the ZFC and FC magnetization curves overlap and suddenly decrease above a certain temperature, which is identified as the Néel temperature, T_N, of the AFM core of each sample. The measured T_N of **FeO** core (180 K) is smaller than that of the bulk (198 K) possibly because of the reduction of the exchange coupling due, among others to the structural defects, to the cut-off of the spin-wave length, to size and/or surface effects.[46,47] For **CoFeO** T_N was observed at ≈220–230 K; this value is an intermediate between the T_N of bulk FeO (198 K) and CoO (291 K) and matches very well with that estimated considering the 0.3:0.7 stoichiometric ratio between the two monoxides (226 K), confirming the formation of a mixed metal monoxide core. For **NiCoFeO**, the transition appeared at 260 K. This value is close to that estimated by linear combination of the T_N of the bulk FeO, CoO, and NiO weighted for the stoichiometry derived experimentally (273 K). In addition, a shoulder at ≈50–60 K was observed in all the curves. By analogy to a similar effect previously observed in Fe_3O_4 and γ-Fe_2O_3 nanocrystals,[48–51] this shoulder was tentatively attributed to spin-glass-like freezing arising from the partially disordered ferrite shell around the monoxide. However, further measurements are required in order to confirm the attribution.

For **FeO** and **CoFeO** the temperature dependence of the ZFC and FC magnetization measured applying a lower field (5 mT) still displays the magnetic transition of the AFM core, while no evidence of such transition is observed for **NiCoFeO** (Figure 7b, red symbols), probably because it overlaps with the superparamagnetic transition appearing above 350 K (see below). Interestingly, these curves also exhibit some features characteristic of the FiM shell. Indeed, for **FeO** NPs (black dots) a broad peak is observed at 120 K that can be attributed to the Verwey transition[52] of the magnetite shell. Moreover, in all the cases, the ZFC-FC curves do not overlap till the maximum reached temperature, that is higher than the T_N of the AFM cores. This irreversible magnetic behavior is a fingerprint of the blocked state of the FiM shells in all the investigated temperature range and hence also at room temperature.

A smooth magnetization reversal process was observed in the hysteresis loops of the 3 samples recorded at 300 and 5 K (**Figure 8**a,b). The absence of a step in these magnetization isotherms indicated a strong exchange coupling between the monoxide and the ferrite phases in the CS. The main magnetic parameters extracted from the loops are reported in **Table 2**. The substitution of $Fe^{(II)}$ for $Co^{(II)}$ and $Ni^{(II)}$ in the ferrimagnetic shell of **CoFeO** and **NiCoFeO** NPs caused a marked decrease of M_{5T} of the doped samples, both at low and room temperature. The difference of the magnetization values cannot be explained only by the higher FiM volume shell in the **FeO** sample (25% bigger than the doped samples), but it can be also attributed to the increase of the magnetic disorder in the shell of the doped samples, as it is explained below. The room temperature coercive field and the remanent magnetization, were negligible for **FeO** and increased with the amount of $Co^{(II)}$ doping. Surprisingly, at 5 K, the coercive field of **CoFeO** is lower than that of **FeO** and **NiCoFeO**. This may be due to the higher relative contribution of the AFM component, evidenced by the linear behavior of the magnetization for fields higher than 1 T. The dominant role of AFM component in the CS **CoFeO** NPs can be ascribed to the large magnetic disorder in the shell. We hypothesized that this disorder is due to the large amount of $Co^{(II)}$ that prevented the formation of a well-defined S structure after the controlled mild oxidation step. Thus, such disorder makes the
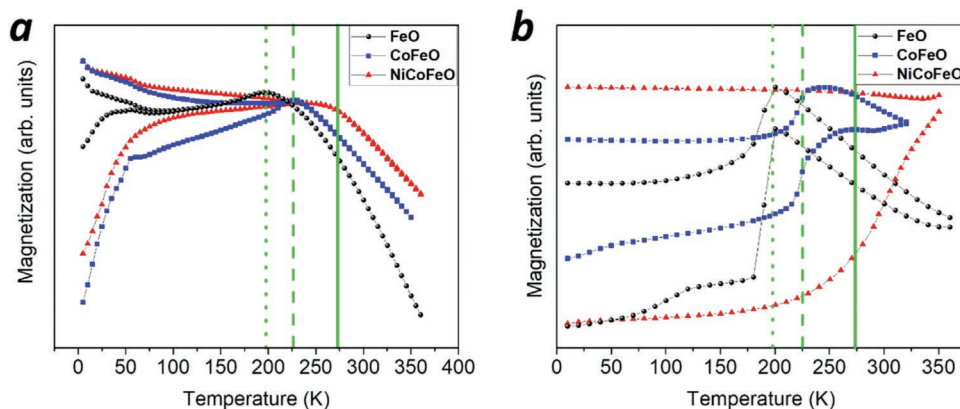

Figure 7. Temperature dependence of the magnetization recorded after ZFC and FC procedures, applying a static field of a) 5 T and b) 5 mT. Black dots, blue squares, and red triangles denote magnetization of **FeO**, **CoFeO**, and **NiCoFeO**, respectively. The green dotted, dashed, and solid lines are the reference Néel temperature for FeO (198 K), CoFeO (226 K), and NiCoFeO (273 K), estimated considering the experimental stoichiometries and the bulk T_N for FeO (198 K), CoO (291 K), and NiO (525 K).
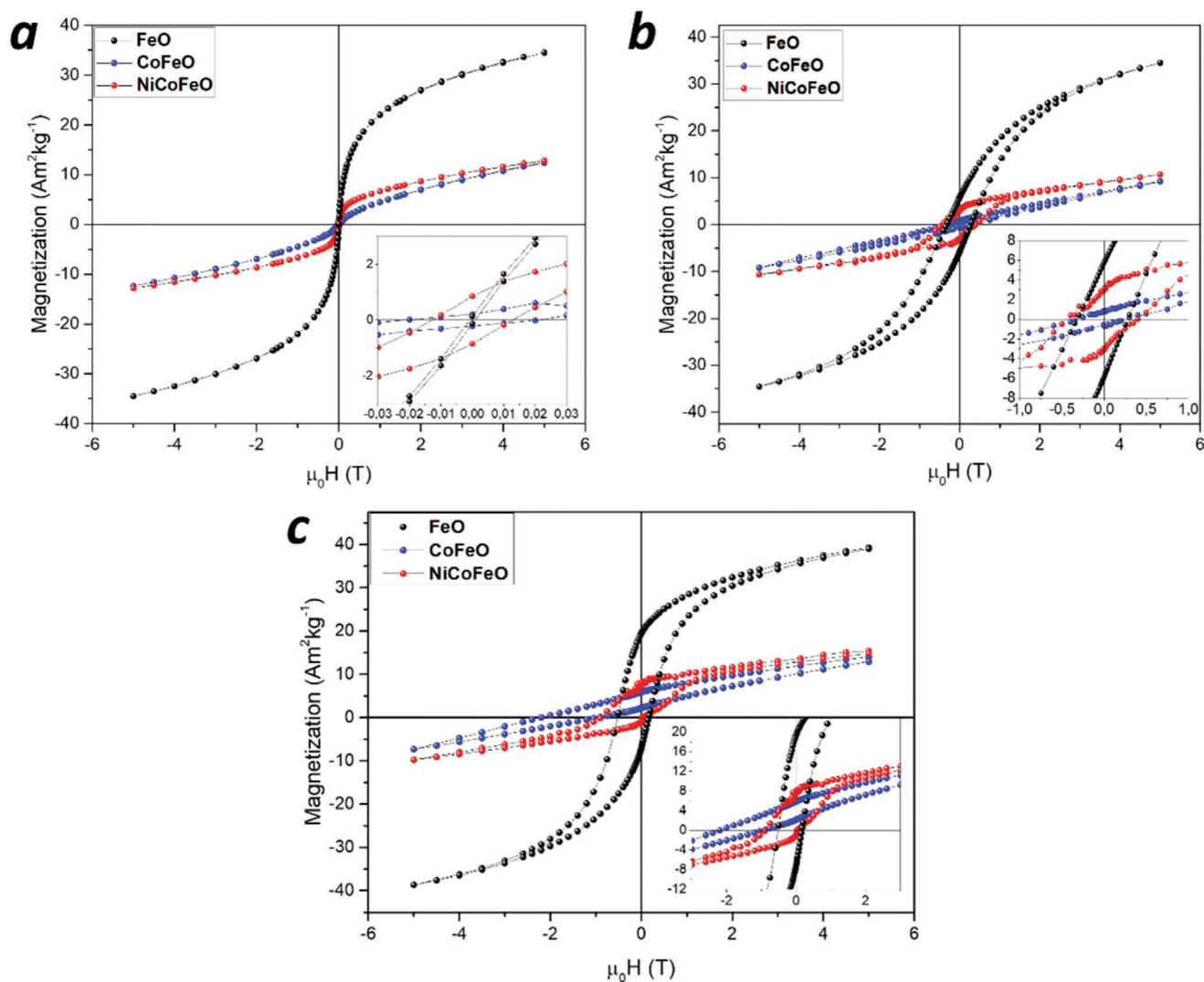
**ADVANCED
SCIENCE NEWS**

www.advancedsciencenews.com

NANO · MICRO

small

www.small-journal.com

Figure 8. Hysteresis loops of **FeO** (black symbols), **CoFeO** (blue symbols), and **NiCoFeO** (red symbols), measured at: a) 300 k, b) 5 K, and c) 5 K after a 5 T FC procedure. The insets show the low field regions of the loops.

relative contribution of the FiM component less important in **CoFeO** than in the other two samples. This feature is clearly evidenced in the 5 K magnetization loops by subtracting the AFM contribution, estimated by a linear fit of the high field magnetization values. The obtained curves, representative of the FiM shell magnetization, are reported in the Supporting

Information. The highest value of the coercivity of the shell, $\mu_0H_C^{FiM}$, was observed for **CoFeO**, in agreement with the higher amount of $Co^{(II)}$ in the S lattice, which increases the total magnetic anisotropy of the NPs. After the removal of the linear contribution, the squareness of the loop is also increased, the reduced remanence magnetization being 0.57. Interestingly, the

Table 2. Magnetization at 5 T, M_{5T}; remanence, M_R (reduced remanence, $R\%$, in brackets); coercive field, μ_0H_C; and exchange bias $\mu_0H_E = (\mu_0H_C^+ + \mu_0H_C^-)/2$; at 5 K, 300 K, and 5 K after a FC procedure. The FC coercivity was estimated as $\mu_0H_C^{FC} = (\mu_0H_C^+ - \mu_0H_C^-)/2$. The magnetization values are normalized to the weight of the inorganic component. The errors for M_S, M_R, and μ_0H_C have been assessed to be 2% of the experimental values.

Sample	5 K			300 K			5 K_FC 5 T			
	M_{5T} [Am² kg⁻¹]	M_R (R%) [Am² kg⁻¹]	μ_0H_C [T]	M_{5T} [Am² kg⁻¹]	M_R (R%) [Am² kg⁻¹]	μ_0H_C [T]	M_{5T} [Am² kg⁻¹]	M_R (R%) [Am² kg⁻¹]	$\mu_0H_C^{FC}$ [T]	μ_0H_E [T]
FeO	35	6 (17)	0.32	35	0.1 (0.3)	0.001	39	20 (51)	0.3	0.2
CoFeO	9	0.8 (9)	0.27	12	0.2 (2)	0.02	14	6 (43)	0.6	1.6
NiCoFeO	11	3 (30)	0.44	13	1 (8)	0.01	15	8 (53)	0.5	0.5

**ADVANCED
SCIENCE NEWS**

www.advancedsciencenews.com

**NANO · MICRO
small**

www.small-journal.com

shape of the **NiCoFeO** hysteresis loop displays a much more pronounced F(i)M-like character than in **CoFeO**, suggesting that Ni$^{(II)}$ induces a partial recovery of the magnetic order in the shell lattice (Figure S6, Supporting Information).

With the aim of quantifying the exchange bias effect, the hysteresis loops at 5 K were measured after a FC process from 360 K, applying a 5 T magnetic field (Figure 8c). The magnetization loops of **CoFeO** and **NiCoFeO** are shifted to the left (exchange bias effect) and upward, and are not fully reversible, since at 5 T the magnetization does not recover the initial value after a whole cycle. The high anisotropy field (the external applied field, H, is lower than the material's intrinsic anisotropy field, H_A), of the doped samples (induced by the strong AFM component), implies that the measurement is carried out in a minor loop and this can lead to a vertical shift due to the residual magnetization after the FC procedure.[53] On the other hand, the spin pinning at the interface, responsible of the exchange bias effect, can also induce a vertical shift.[54] In our case, the larger contribution to the vertical shift is ascribable to the minor loop effect ($H_A > H$ makes that part of the magnetization aligned with the field is no more switched). Recording loops with higher applied magnetic field, indeed, the vertical shift is reduced (see Supporting Information). These features are predominant in the **CoFeO** NPs, where $\mu_0 H_C^{FC}$ and $\mu_0 H_E$, that is, the parameters characterizing the exchange bias effect, increased by ≈90% and decreased by ≈60%, respectively, after applying 12 T (Table 2; Figure S7b, Supporting Information).

The results reported so far highlight that the co-doping with two different divalent cations (Co$^{(II)}$ and Ni$^{(II)}$) is a good strategy for modulating the magnetic properties of iron oxide CS NPs. Indeed, while cobalt doping leads to an enhancement of anisotropy and bias effect, the presence of nickel ions allows to partially recover the magnetic order in the shell and to enhance the AFM ordering transition temperature up to 260 K, so that the final nano-heterostructure exhibits improved T_N, remanence, and squareness with respect to those observed in **CoFeO**, and much larger coercivity and bias than those observed in **FeO**. It is worth to note that this strategy can be used to shift the T_N toward room temperature. A further increase of T_N, indeed, was achieved by raising the Co$^{(II)}$ and Ni$^{(II)}$ content in the metal precursor above the ratio Fe:(Co, Ni) 2:1, and thus decreasing the stoichiometric amount of Fe$^{(III)}$. As clearly shown by the ZFC/FC magnetization curves at 5 mT (Figure S8, Supporting Information), the as synthesized nickel-cobalt doped iron monoxide with stoichiometry Ni$_{0.18}$Co$_{0.22}$Fe$_{0.60}$O@Ni$_{0.5}$Co$_{0.7}$Fe$_{1.8}$O$_4$ exhibits T_N at ≈280 K. As expected, this enhances the exchange bias effect with respect to **NiCoFeO** and makes it appearing at temperatures closer to room temperature (see Figure S9, Supporting Information)

3. Conclusions

In the present work, we investigated the structural and magnetic properties of AFM@FiM CS NPs of composition Fe$_{0.95}$O@Fe$_3$O$_4$, Co$_{0.3}$Fe$_{0.7}$O@Co$_{0.8}$Fe$_{2.2}$O$_4$, and Ni$_{0.17}$Co$_{0.21}$Fe$_{0.62}$O@Ni$_{0.4}$Co$_{0.3}$Fe$_{2.3}$O$_4$, mean diameter of ≈20 nm and well-defined interface. The CS architecture was obtained by partially controlled oxidation of the monoxide core surface. The

thicker ferrite shell obtained for the wüstite NPs highlighted the higher stability toward the oxidation process in ambient conditions attained when Ni$^{(II)}$ and/or Co$^{(II)}$ ions are included in the iron oxide lattice.

The introduction of cobalt and nickel induced an increase of the magnetic anisotropy and of the exchange bias. Moreover, the addition of Ni$^{(II)}$ in the lattice led to the formation of a more ordered ferrite shell which increased the magnetization at 5 T and the remanence compared to **CoFeO** NPs. These results point out that the co-doping with the two divalent ions allows a good compromise between the increase of the anisotropy and exchange bias due to Co-doping, and the decrease of the remanence associated to the Fe$^{(II)}$ replacement with Ni$^{(II)}$. **NiCoFeO** NPs, indeed, exhibit much larger coercivity and bias than **FeO** and a higher T_N (260 K), remanence, and hysteresis loop squareness with respect to those observed in **CoFeO** NPs. A further increase of the T_N, up to ≈280 K was obtained by decreasing the amount of the iron below the stochiometric Fe:(Co, Ni) 2:1 ratio. This study demonstrates how 3d metal doping is effective to tune the chemical-physical properties of this new material. In particular, the shifting of T_N close to room temperature leads to an exchange bias material suitable for technological applications or as building blocks for the synthesis of rare earth-free permanent magnets.

4. Experimental Section

Chemicals and Materials: Iron(III) chloride hexahydrate (FeCl$_3$·6H$_2$O, 98% from Sigma Aldrich), Cobalt(II) chloride hexahydrate (CoCl$_2$·6H$_2$O, 98% from Honeywell), Nickel(II) chloride (NiCl$_2$·6H$_2$O, 98% from Sigma Aldrich), oleic acid (OA, 90%, Aldrich), docosane (97%, Aldrich), ethanol (99.8%, Fluka), hexane (99%, Honeywell), and 2-propanol (98%, Honeywell) were used without any further purification.

Oleate Precursors Synthesis: Iron oleate (Fe(OL)) precursor was synthesized by dissolving FeCl$_3$·6H$_2$O in 20 mL of hexane, 10 mL of ethanol, and 10 mL of distilled water. At room temperature, stoichiometric amount of NaOL was added and the mixture was heated at 75 °C, under vigorous stirring, for 5 h. The brown colored organic phase was separated from the aqueous phase and a brown-dark waxy product was obtained after solvent evaporation. The same procedure was adopted for the synthesis of cobalt–iron oleate, CoFe(OL), (metal chloride molar ratio of 0.33:0.67) and nickel–cobalt–iron oleate, NiCoFe(OL), (metal chloride molar ratio of 0.13:0.20:0.67). The stoichiometry of the final products was confirmed by inductively coupled plasma analysis. For the cobalt-doped sample, the metal ratio was chosen to get the highest magnetic anisotropy shell, which corresponded to the non-stoichiometric cobalt ferrite, Co$_x$Fe$_{3-x}$O$_4$ with x = 0.5–0.8.[25,55] The composition of the RS core was tuned accordingly, based on the authors' previous work on this kind of systems.[56] For **NiCoFeO** the precursor composition was chosen by preparing a series of samples with variable Ni:Co ratio, and the same Fe content of **CoFeO**. The selected metal stoichiometry corresponded to the best compromise between high intrinsic magnetic anisotropy (due to Co^{2+}) and T_N (due to Ni^{2+}).

Synthesis of Fe$_{1-x}$O@Fe$_3$O$_4$ (FeO) core@shell NPs: The Fe$_{1-x}$O NPs were synthesized by thermal decomposition of the metal precursor. 0.9 g (1 mmol) of Fe(OL) and 0.33 g (1.1 mmol) of OA were dissolved in 7 mL of docosane at 80 °C. The mixture was heated from 80 to 330 °C, at 2.5 °C min^{-1}, under vigorous stirring and nitrogen flux. The suspension was kept at 330 °C for 30 min and then let cool down to room temperature. The resulting black powder was separated by applying an external magnet, washed with 2-propanol and ethanol, and finally dried under nitrogen flux. The Fe$_{1-x}$O@Fe$_3$O$_4$ CS architecture was obtained by oxidation of the Fe$_{1-x}$O surface during the washing step.

2107426 (9 of 11)

ADVANCED
SCIENCE NEWS

www.advancedsciencenews.com

NANO · MICRO
small

www.small-journal.com

Synthesis of $Co_xFe_{1-x}O@Co_yFe_{3-y}O_4$ (CoFeO) and $Ni_zCo_xFe_{1-x-z}O@Ni_wCo_yFe_{3-w-y}O_4$ (NiCoFeO) core@shell NPs: The doped monoxide NPs were synthesized by thermal decomposition of the corresponding metal precursors. In a typical synthesis, 1.5 g (2 mmol) of CoFe(OL) and 0.57 g (2 mmol) of OA for **CoFeO** or 1.5 g (2 mmol) of NiCoFe(OL) and 2.5 g (9 mmol) of OA for **NiCoFeO**, were dissolved in 10 mL of docosane at 80 °C. The mixture was heated from 80 to 330 °C, at 2.5 °C min⁻¹, under vigorous stirring and nitrogen flux. The suspension was kept at 330 °C for 40 min and then let cool down to room temperature. The resulting black powder was washed following the same procedure already explained above for the synthesis of **FeO**. For both samples the CS architecture was obtained by partial controlled oxidation of the NPs surface during the washing step.

Characterization Techniques: Powder XRD data were recorded using a Bruker New D8 ADVANCE ECO diffractometer equipped with a Cu Kα (1.5406 Å) radiation source and operating in θ–θ Bragg–Brentano geometry at 40 kV and 40 mA. The measurements were carried out in the range 25°–70°, with step size of 0.03° and collection time of 1 s. ED patterns were acquired on a ThermoFischer Talos F200S G2 TEM/STEM at a camera length of 840 mm with a condenser aperture of 70 μm and a selective area aperture of 40 μm, to assure an almost parallel beam. The same conditions of excitations of the condenser lens (intensity) and of the objective lens (focus) were used for all the samples, to allow the comparison of the different diffractions patterns and to reduce the errors in the derived plane distances as much as possible. An aluminum polycrystalline sample (Agar Scientific) was used for pixel calibration of the diffraction patterns. Azimuthal integration of the diffraction patterns was performed after careful measurement of the center of the diffraction patterns. The obtained profiles were analyzed by using the PASAD plugin for Digital Micrograph (Gatan, Inc.). TEM (CM12 Philips equipped with a LaB6 filament operating at 100 kV) was employed to determine morphology and size distribution of the NPs. The mean diameter and the NPs size distribution for each sample were obtained by statistical analysis over more than 100 NPs, using the Image Pro-Plus and the Origin software. STEM images were acquired on a probe-corrected Titan (Thermo Fischer Scientific), with a working voltage of 300 kV. The microscope was equipped with a high annular dark field detector for imaging (Fischione) and an energy filter (Gatan, Inc.) for EELS mapping. For the measurements, a convergence angle of 24.8 mrad and a collection angle of 51.3 mrad, were used. To obtain the crystalline structure of the different phases present in the system, an image-corrected Titan3 (Thermo Fischer Scientific) UHRTEM was operated at 300 kV. The transition metal content (w/w) in NPs was assessed by using an EDXRF spectrometer Shimadzu EDX-7000.

Elemental analysis was performed in triplicate by a PerkinElmer Optima 2000 Perkin Elmer Inductively Coupled Plasma-Optical Emission Spectrophotometer Dual Vision. The amount of organic ligand on the surface of NPs was determined by CHN analysis with an Elemental Analyzer CHN-S Flash E1112 Thermofinnigan. Magnetization response as a function of the temperature and of the field up to 5 T was investigated on randomly oriented pressed powder pellets using a Quantum Design MPMS SQUID magnetometer. Hysteresis loop at 9 T was recorded using a Quantum Design PPMS magnetometer, equipped with a vibrating sample magnetometer (VSM). Hysteresis loop at 12 T was recorded using a VSM Oxford Instrument MAGLAB2000 magnetometer. The field was always applied perpendicular to the normal of the pellets.

Supporting Information

Supporting Information is available from the Wiley Online Library or from the author.

Conflict of Interest

The authors declare no conflict of interest.

Data Availability Statement

The data that support the findings of this study are available from the corresponding author upon reasonable request.

[1] M. Sanna Angotzi, V. Mameli, C. Cara, A. Musinu, C. Sangregorio, D. Niznansky, H. L. L. Xin, J. Vejpravova, *Nanoscale Adv.* **2020**, *2*, 3191.

[2] M. G. Sibi, D. Verma, J. Kim, *Catal. Rev.: Sci. Eng.* **2019**, *62*, 163.

[3] D. Rawat, P. B. Barman, R. R. Singh, *Sci. Rep.* **2019**, *9*, 9.

[4] K. Sartori, G. Cotin, C. Bouillet, V. Halté, S. Bégin-Colin, F. Choueikani, B. P. Pichon, *Nanoscale* **2019**, *11*, 12946.

[5] J. Nogués, I. K. Schuller, *J. Magn. Magn. Mater.* **1999**, *192*, 203.

[6] H. Khurshid, S. Chandra, W. Li, M. H. Phan, G. C. Hadjipanayis, P. Mukherjee, H. Srikanth, *J. Appl. Phys.* **2013**, *113*, 17B508.

[7] A. Lak, M. Kraken, F. Ludwig, A. Kornowski, D. Eberbeck, S. Sievers, F. J. Litterst, H. Weller, M. Schilling, *Nanoscale* **2013**, *5*, 12286.

[8] X. Sun, N. Frey Huls, A. Sigdel, S. Sun, *Nano Lett.* **2012**, *12*, 246.

[9] J. Park, J. Joo, S. G. Kwon, Y. Jang, T. Hyeon, *Angew. Chem., Int. Ed.* **2007**, *46*, 4630.

[10] L. M. Bronstein, X. L Huang, J. Retrum, A. Schmucker, M. Pink, B. D. Stein, B. Dragnea, *Chem. Mater.* **2007**, *19*, 3624.

[11] A. López-Ortega, E. Lottini, G. Bertoni, C. De Julián Fernández, C. Sangregorio, *Chem. Mater.* **2017**, *29*, 1279.

[12] J. Chen, S. Peng, D. Xiong, H. Cheng, H. Zhou, Y. Jiang, J. Lu, W. Li, W. Zhao, *J. Phys. D* **2020**, *53*, 334001.

[13] J. Zhang, J. Zhou, Z. L. Luo, Y. B. Chen, J. Zhou, W. Lin, M. H. Lu, S. T. Zhang, C. Gao, D. Wu, Y. F. Chen, *Phys. Rev. B* **2020**, *101*, 014422.

[14] J. H. Chang, D. Hahm, K. Char, W. K. Bae, *J. Inf. Disp.* **2017**, *18*, 57.

[15] R. F. L. Evans, D. Bate, R. W. Chantrell, R. Yanes, O. Chubykalo-Fesenko, *Phys. Rev. B* **2011**, *84*, 092404.

[16] R. F. L. Evans, R. W. Chantrell, O. Chubykalo-Fesenko, *MRS Bull.* **2013**, *38*, 909.

[17] C. Leighton, J. Nogués, B. J. Jönsson-Åkerman, I. K. Schuller, *Phys. Rev. Lett.* **2000**, *84*, 3466.

[18] L. Jelver, P. M. Larsen, D. Stradi, K. Stokbro, K. W. Jacobsen, *Phys. Rev. B* **2017**, *96*, 085306.

[19] D. Meggiolaro, E. Mosconi, A. H. Proppe, R. Quintero-Bermudez, S. O. Kelley, E. H. Sargent, F. De Angelis, *ACS Energy Lett.* **2019**, *4*, 2181.

[20] Y. Hou, Z. Xu, S. Sun, *Angew. Chem., Int. Ed.* **2007**, *46*, 6329.

[21] H. Khurshid, W. Li, S. Chandra, M. H. Phan, G. C. Hadjipanayis, P. Mukherjee, H. Srikanth, *Nanoscale* **2013**, *5*, 7942.

[22] D. W. Kavich, J. H. Dickerson, S. V. Mahajan, S. A. Hasan, J. H. Park, *Phys. Rev. B: Condens. Matter Mater. Phys.* **2008**, *78*, 174414.

[23] J. Liu, Y. Z. Bin, M. Matsuo, *J. Phys. Chem. C* **2012**, *116*, 134.

[24] S. Anjum, R. Tufail, H. Saleem, R. Zia, S. Riaz, *J. Supercond. Nov. Magn.* **2017**, *30*, 2291.

[25] E. Fantechi, G. Campo, D. Carta, A. Corrias, C. De Julián Fernández, D. Gatteschi, C. Innocenti, F. Pineider, F. Rugi, C. Sangregorio, *J. Phys. Chem. C* **2012**, *116*, 8261.

[26] V. Mameli, A. Musinu, A. Ardu, G. Ennas, D. Peddis, D. Niznansky, C. Sangregorio, C. Innocenti, N. T. K. Thanh, C. Cannas, *Nanoscale* **2016**, *8*, 10124.

[27] A. Mandziak, G. D. Soria, J. E. Prieto, P. Prieto, C. Granados-Miralles, A. Quesada, M. Foerster, L. Aballe, J. de la Figuera, *Sci. Rep.* **2019**, *9*, 13584.

[28] E. Lottini, A. López-Ortega, G. Bertoni, S. Turner, M. Meledina, G. Van Tendeloo, C. De Julián Fernández, C. Sangregorio, *Chem. Mater.* **2016**, *28*, 4214.

[29] P. Tancredi, P. C. R. Rojas, O. Moscoso-Londoño, U. Wolff, V. Neu, C. Damm, B. Rellinghaus, M. Knobel, L. M. Socolovsky, *New J. Chem.* **2017**, *41*, 15033.

[30] J. M. D. Coey, *Magnetism and Magnetic Materials*, Cambridge University Press, Cambridge **2010**.

[31] M. J. Carey, A. E. Berkowitz, *Appl. Phys. Lett.* **1992**, *60*, 3060.

[32] J. Khemprasit, S. Kaen-Ngam, B. Khumpaitool, P. Kamkhou, *J. Magn. Magn. Mater.* **2011**, *323*, 2408.

[33] A. Lappas, G. Antonaropoulos, K. Brintakis, M. Vasilakaki, K. N. Trohidou, V. Iannotti, G. Ausanio, A. Kostopoulou, M. Abeykoon, I. K. Robinson, E. S. Bozin, *Phys. Rev. X* **2019**, *9*, 041044.

[34] E. Wetterskog, C. W. Tai, J. Grins, L. Bergström, G. Salazar-Alvarez, *ACS Nano* **2013**, *7*, 7132.

[35] G. Lucas, P. Burdet, M. Cantoni, C. Hébert, *Micron* **2013**, *52*, 49.

[36] C. Gammer, C. Mangler, C. Rentenberger, H. P. Karnthaler, *Scr. Mater.* **2010**, *63*, 312.

[37] G. S. Pawley, *J. Appl. Crystallogr.* **1981**, *14*, 357.

[38] A. Yamamoto, *Acta Crystallogr. B* **1982**, *38*, 1451.

[39] H. W. King, Y. Lo Vegard, *J. Mater. Sci.* **1921**, *1*, 79.

[40] R. Kannan, M. S. Seehra, *Phys. Rev. B* **1987**, *35*, 6847.

[41] C. J. Ksanda, *Am. J. Sci.* **1931**, *22*, 131.

[42] M. Estrader, A. López-Ortega, I. V. Golosovsky, S. Estradé, A. G. Roca, G. Salazar-Alvarez, L. López-Conesa, D. Tobia, E. Winkler, J. D. Ardisson, W. A. A. Macedo, A. Morphis, M. Vasilakaki, K. N. Trohidou, A. Gukasov, I. Mirebeau, O. L. Makarova, R. D. Zysler, F. Peiró, M. D. Baró, L. Bergström, J. Nogués, *Nanoscale* **2015**, *7*, 3002.

[43] B. P. Pichon, O. Gerber, C. Lefevre, I. Florea, S. Fleutot, W. Baaziz, M. Pauly, M. Ohlmann, C. Ulhaq, O. Ersen, V. Pierron-Bohnes, P. Panissod, M. Drillon, S. Begin-Colin, *Chem. Mater.* **2011**, *23*, 2886.

[44] S. V. Bhandare, R. Kumar, A. V. Anupama, H. K. Choudhary, V. M. Jali, B. Sahoo, *J. Magn. Magn. Mater.* **2017**, *433*, 29.

[45] J. Zhang, S. Zhu, H. Li, L. Zhu, Y. Hu, W. Xia, X. Zhang, Y. Peng, J. Fu, *Nanoscale* **2018**, *10*, 10123.

[46] J.-V. Kim, R. L. Stamps, *Appl. Phys. Lett.* **2001**, *79*, 2785.

[47] M. R. Ghadimi, B. Beschoten, G. Güntherodt, *Appl. Phys. Lett.* **2005**, *87*, 261903.

[48] M. Suzuki, S. I. Fullem, I. S. Suzuki, L. Y. Wang, C. J. Zhong, *Phys. Rev. B: Condens. Matter Mater. Phys.* **2009**, *79*, 024418.

[49] H. Wang, T. Zhu, K. Zhao, W. N. Wang, C. S. Wang, Y. J. Wang, W. S. Zhan, *Phys. Rev. B* **2004**, *70*, 092409.

[50] H. Khurshid, P. Lampen-Kelley, Ò. Iglesias, J. Alonso, M. H. Phan, C. J. Sun, M. L. Saboungi, H. Srikanth, *Sci. Rep.* **2015**, *5*, 15054.

[51] C. S. Olson, C. L. Heth, F. L. Alema, S. H. Lapidus, P. W. Stephens, K. I. Pokhodnya, *J. Phys. Condens. Matter* **2013**, *25*, 256004.

[52] E. J. W. Verwey, *Nature* **1939**, *144*, 327.

[53] J. Geshev, *J. Magn. Magn. Mater.* **2008**, *320*, 600.

[54] M. Kaur, J. S. McCloy, Y. Qiang, *J. Appl. Phys.* **2013**, *113*, 17D715.

[55] M. Tachiki, *Prog. Theor. Phys.* **1960**, *23*, 1055.

[56] E. Lottini 2016, 145.